

A Mechanistic Model for Carbon Dioxide Corrosion of Mild Steel in the Presence of Protective Iron Carbonate Films—Part 1: Theory and Verification

M. Nordsveen,* S. Nešić,[†]** R. Nyborg,*** and A. Stangeland****

ABSTRACT

A mechanistic model of uniform carbon dioxide (CO₂) corrosion is presented that covers the following: electrochemical reactions at the steel surface, diffusion of species between the metal surface and the bulk including diffusion through porous surface films, migration due to establishment of potential gradients, and homogenous chemical reactions including precipitation of surface films. The model can predict the corrosion rate as well as the concentration and flux profiles for all species involved. Comparisons with laboratory experiments have revealed the strengths of the model such as its ability to assist in understanding complex processes taking place during corrosion in the presence of surface films.

KEY WORDS: carbon dioxide, carbon dioxide corrosion, carbon steel, model, prediction, protective films

INTRODUCTION

Numerous prediction models for carbon dioxide (CO₂) corrosion of carbon steel exist.¹⁻¹⁹ Most of these are semiempirical, while some of the more recent models are based on mechanistic descriptions of the pro-

cesses underlying CO₂ corrosion.¹⁴⁻¹⁹ A thorough review of the field of CO₂ corrosion modeling was published in 1997.²⁰ A joint industry project where several of the models were compared with actual field data recently has been finished.²¹ The present study describes another attempt at mechanistic modeling in which some of the deficiencies noted in the previously published works are addressed. The significance of the present study is that it mathematically models most of the important processes present in corrosion using fundamental physicochemical laws. Therefore, even if the model was created primarily to cover the area of uniform CO₂ corrosion, it can, with small modifications, be adapted to cover various other types of corrosion, by addition/removal of species and corresponding chemical and electrochemical reactions.

The following section covering the physicochemical model describes qualitatively all the processes underlying CO₂ corrosion and lists all the relevant chemical and electrochemical reactions. It describes how CO₂ corrosion happens, without referring to complex equations. The section on the mathematical model displays how these concepts are cast into equations. The section on the numerical methods discusses means of solving these equations. The section on verification shows how the model predictions compare with results of experimental laboratory studies. Finally, the last section on numerical experimentation foreshadows how a mechanistic model such as this one can be used to help understand and control CO₂ corrosion. This aspect of the model is elaborated on in the second part of this study.

Submitted for publication October 2001; in revised form, December 2002. Presented as paper no. 01040 at CORROSION/2001, March 2001, Houston, TX.

[†] Corresponding author.

* Institute for Energy Technology, N-2027 Kjeller, Norway. Present address: Scandpower AS, PO Box 3, 2027 Kjeller, Norway.

** Institute for Energy Technology, N-2027 Kjeller, Norway. Present address: Institute for Corrosion and Multiphase Flow Technology, Chemical Engineering Department, Ohio University, 340 1/2 W. State St., Stocker Center, Athens, OH 45701. E-mail: nesic@bobcat.ent.ohiou.edu.

*** Institute for Energy Technology, N-2027 Kjeller, Norway.

**** Institute for Energy Technology, N-2027 Kjeller, Norway. Present address: GE Energy Norway, PO Box 443, 1327 Lysaker, Norway.

TABLE 1
Chemical Reactions Accounted for in the Model and Their Equilibrium Constants

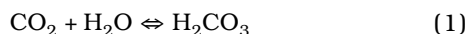
	Reaction	Equilibrium Constant
Dissolution of carbon dioxide	$\text{CO}_2(\text{g}) \rightleftharpoons \text{CO}_2$	$K_{\text{sol}} = c_{\text{CO}_2}/p_{\text{CO}_2}$
Water dissociation	$\text{H}_2\text{O} \xrightleftharpoons[k_{\text{b,wa}}]{k_{\text{f,wa}}} \text{H}^+ + \text{OH}^-$	$K_{\text{wa}} = c_{\text{H}^+}c_{\text{OH}^-}$
Carbon dioxide hydration	$\text{CO}_2 + \text{H}_2\text{O} \xrightleftharpoons[k_{\text{b,hy}}]{k_{\text{f,hy}}} \text{H}_2\text{CO}_3$	$K_{\text{hy}} = c_{\text{H}_2\text{CO}_3}/c_{\text{CO}_2}$
Carbonic acid dissociation	$\text{H}_2\text{CO}_3 \xrightleftharpoons[k_{\text{b,ca}}]{k_{\text{f,ca}}} \text{H}^+ + \text{HCO}_3^-$	$K_{\text{ca}} = c_{\text{H}^+}c_{\text{HCO}_3^-}/c_{\text{H}_2\text{CO}_3}$
Biocarbonate anion dissociation	$\text{HCO}_3^- \xrightleftharpoons[k_{\text{b,bi}}]{k_{\text{f,bi}}} \text{H}^+ + \text{CO}_3^{2-}$	$K_{\text{bi}} = c_{\text{H}^+}c_{\text{CO}_3^{2-}}/c_{\text{HCO}_3^-}$
Dissolution of hydrogen sulfide	$\text{H}_2\text{S}(\text{g}) \rightleftharpoons \text{H}_2\text{S}$	$K_{\text{H}_2\text{S,sol}} = c_{\text{H}_2\text{S}}/p_{\text{H}_2\text{S}}$
Hydrogen sulfide dissociation	$\text{H}_2\text{S} \xrightleftharpoons[k_{\text{b,H}_2\text{S}}]{k_{\text{f,H}_2\text{S}}} \text{H}^+ + \text{HS}^-$	$K_{\text{H}_2\text{S}} = c_{\text{H}^+}c_{\text{HS}^-}/c_{\text{H}_2\text{S}}$
Hydrogen sulfide anion dissociation	$\text{HS}^- \xrightleftharpoons[k_{\text{b,HS}^-}]{k_{\text{f,HS}^-}} \text{H}^+ + \text{S}^{2-}$	$K_{\text{HS}^-} = c_{\text{H}^+}c_{\text{S}^{2-}}/c_{\text{HS}^-}$
Acetic acid dissociation	$\text{HAc} \xrightleftharpoons[k_{\text{b,ac}}]{k_{\text{f,ac}}} \text{H}^+ + \text{Ac}^-$	$K_{\text{HAc}} = c_{\text{H}^+}c_{\text{Ac}^-}/c_{\text{HAc}}$
Hydrogen sulfate anion dissociation	$\text{HSO}_4^- \xrightleftharpoons[k_{\text{b,HSO}_4^-}]{k_{\text{f,HSO}_4^-}} \text{H}^+ + \text{SO}_4^{2-}$	$K_{\text{HSO}_4^-} = c_{\text{H}^+}c_{\text{SO}_4^{2-}}/c_{\text{HSO}_4^-}$
Iron carbonate precipitation	$\text{Fe}^{2+} + \text{CO}_3^{2-} \rightleftharpoons \text{FeCO}_3$	$K_{\text{sp}} = c_{\text{Fe}^{2+}}c_{\text{CO}_3^{2-}}$

PHYSICO-CHEMICAL MODEL OF CO_2 CORROSION OF MILD STEEL

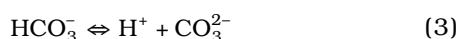
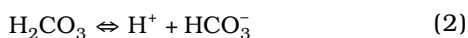
In uniform CO_2 corrosion of mild steel, a number of chemical, electrochemical, and transport processes occur simultaneously. They are briefly described below.

Chemical Reactions

When dissolved in water, CO_2 is hydrated to give carbonic acid (H_2CO_3):



which then dissociates in two steps:



In practical CO_2 corrosion situations, many other species are present in the water solution. Therefore, a large number of additional chemical reactions can occur. The full list of the chemical reactions ac-

counted for in the present version of the model is shown in Table 1.

Chemical reactions are sometimes very fast compared to all other processes occurring simultaneously, thus preserving chemical equilibrium throughout the solution. In other cases, when chemical reactions proceed slowly, other faster processes (such as electrochemical reactions or diffusion) can lead to local nonequilibrium in the solution. Either way the occurrence of chemical reactions can significantly alter the rate of electrochemical processes at the surface and the rate of corrosion. This is particularly true when, as a result of high local concentrations of species, the solubility limit is exceeded and precipitation of surface films occurs. In a precipitation process, heterogeneous nucleation occurs first on the surface of the metal or within the pores of an existing film since homogenous nucleation in the bulk requires a much higher concentration of species. Nucleation is followed by crystalline film growth. Under certain conditions, surface films can become very protective and reduce the rate of corrosion by forming a transport barrier for the species involved in the corrosion reaction and by covering (blocking) parts of the metal surface (i.e., by making it "unavailable" for corrosion).

In CO₂ corrosion, which is considered here, when the concentrations of Fe²⁺ and CO₃²⁻ ions exceed the solubility limit, they combine to form solid iron carbonate (FeCO₃) films according to:



A number of recent publications discuss the role of FeCO₃ films in CO₂ corrosion.²²⁻²⁴

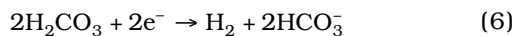
Electrochemical Reactions at the Steel Surface

The presence of CO₂ increases the rate of corrosion of mild steel in aqueous solutions primarily by increasing the rate of the hydrogen evolution reaction. In strong acids, which are fully dissociated, the rate of hydrogen evolution occurs according to:



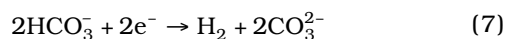
and cannot exceed the rate at which H⁺ ions are transported to the surface from the bulk solution (mass transfer limit). In CO₂ solutions, where typically pH >4, this limiting flux of H⁺ ions is small; therefore, it is the presence of H₂CO₃ that enables hydrogen evolution at a much higher rate. Thus, for pH >4 the presence of CO₂ leads to a much higher corrosion rate than would be found in a solution of a strong acid at the same pH.

The presence of H₂CO₃ can increase the corrosion rate in two different ways. Dissociation of H₂CO₃, as given by Reaction (2), serves as an additional source of H⁺ ions,⁴ which are subsequently reduced according to Equation (5). In addition, there is a possibility that direct reduction of H₂CO₃ can increase the corrosion rate further:



as assumed by many workers in the field.^{1,25-26} Both of these reaction mechanisms for hydrogen evolution have been included in the present model. The direct reduction of H₂CO₃ can be "switched on or off" in the model to study the effect of this additional cathodic reaction.

It has been suggested²⁷ that in CO₂ solutions at pH >5 the direct reduction of the bicarbonate ion becomes important:



which might be true as the concentration of HCO₃⁻ increases with pH and can exceed that of H₂CO₃. However, it is difficult to experimentally distinguish the effect of this particular reaction mechanism for hydrogen evolution from Equations (5) and (6), and therefore this reaction has not been included in the present model.

Hydrogen evolution by direct reduction of water:



can become important²⁸⁻²⁹ only at CO₂ partial pressure (p_{CO₂}) <<1 bar and pH >5 and is therefore rarely an important factor in practical CO₂ corrosion situations. This reaction was also omitted from the present model.

The electrochemical dissolution of iron in a water solution:



is the dominant anodic reaction in CO₂ corrosion. It has been studied extensively in the past with several multistep mechanisms suggested to explain the various experimental results. Even if the overall anodic reaction (Reaction [9]) does not suggest any dependency on pH, numerous studies have revealed that in strong acidic solutions the reaction order with respect to OH⁻ is between 1 and 2. Measured Tafel slopes are typically 30 mV to 40 mV. This subject, which is controversial with respect to the mechanism, is reviewed in detail by Drazic³⁰ and Lorenz and Heusler.³¹ The anodic dissolution in aqueous CO₂ solutions has not been the subject of detailed mechanistic studies, until recently. The mechanism for strong acids, suggested by Bockris, et al.,³² frequently has been assumed to apply in CO₂ solutions in which typically pH >4.^{1,25,27,33} It was overlooked that the experimental results presented by Bockris, et al.,³² show that the pH dependency decreases rapidly as pH >4, suggesting a change in mechanism or a different rate-determining step. In the present study, the results from a recent study by Nescic, et al.,³⁴ were used and it was confirmed that the anodic dissolution of iron does not depend significantly on OH⁻ concentrations above pH 4; however, it is affected by the presence of CO₂, as previously indicated by Davies and Burstein³⁵ and Videm.³⁶

Transport Processes

From the description of the electrochemical processes it is clear that certain species in the solution will be produced in the solution at the metal surface (e.g., Fe²⁺) while others will be depleted (e.g., H⁺). The established concentration gradients will lead to molecular diffusion of the species toward and away from the surface. In cases when the diffusion processes are much faster than the electrochemical processes, the concentration change at the metal surface will be small. Vice versa, when the diffusion is unable to "keep up" with the speed of the electrochemical reactions, the concentration of species at the metal surface can become very different from the ones in the bulk solution. On the other hand, the rate of the electrochemical processes depends on the species

concentrations at the surface. Therefore, there exists a two-way coupling between the electrochemical processes at the metal surface (corrosion) and processes in the adjacent solution layer (i.e., diffusion in the boundary layer). The same is true for chemical reactions that interact with both the transport and electrochemical processes in a complex way, as will be described.

In most practical systems, the water solution moves with respect to the metal surface. Therefore, the effect of convection on transport processes cannot be ignored. Near-solid surfaces, in the boundary layer, time-averaged convection is parallel to the surface and does not contribute to the transport of species to and from the surface. However, transient turbulent eddies can penetrate deep into the boundary layer and significantly alter the rate of species transport to and from the surface. Very close to the surface no turbulence can survive and the species are transported solely by diffusion and electromigration as described in the following paragraph.

Many of the dissolved species in CO₂ solutions are electrically charged (ions) and have different diffusion coefficients. This means that they diffuse through the solution with different "speeds." Consequently, any diffusion occurring as a result of the existence of concentration gradients will tend to separate the charges.³⁷ This will be opposed by strong, short-range, attraction forces between opposing charges. Therefore, only a small separation of charge can occur, building up to a potential gradient within the solution that will tend to "speed up" the slower diffusing ions and "slow down" the faster ones, a process called electromigration or simply migration.

MATHEMATICAL MODEL

A mathematical model is described that covers all of the previously described processes:

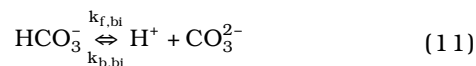
- Homogenous chemical reactions, including precipitation of surface films
- Electrochemical reactions at the steel surface
- Transport of species to and from the bulk, including convection and diffusion through the boundary layer and the porous surface films as well as migration as a result of the establishment of potential gradients

These processes are mathematically modeled using fundamental physicochemical laws and resulting equations. Parameters for the different equations, such as equilibrium constants, reaction rate constants, and diffusion coefficients, are taken from the open literature.

Chemical Reactions

Homogenous chemical reactions can be seen as local sources or sinks of species in the solution. To

describe how the rates of homogenous chemical reactions are calculated, the first and second dissociation steps of H₂CO₃ will be used as an example:



The net rate of change of H₂CO₃ concentration attributable to the first dissociation step—Reaction (10)—is:

$$R_{\text{H}_2\text{CO}_3} = -(k_{f,ca}c_{\text{H}_2\text{CO}_3} - k_{b,ca}c_{\text{H}^+}c_{\text{HCO}_3^-}) \quad (12)$$

where $k_{f,ca}$ and $k_{b,ca}$ are the forward and backward reaction rate constants and $c_{\text{H}_2\text{CO}_3}$, c_{H^+} , and $c_{\text{HCO}_3^-}$ are the concentrations of species involved. In accordance with the law of mass (and electrical charge) conservation, the net rates of change of H⁺ and HCO₃⁻ species concentrations, attributable to the first dissociation step—Reaction (10)—are given by:

$$R_{\text{H}^+} = R_{\text{HCO}_3^-} = -R_{\text{H}_2\text{CO}_3} \quad (13)$$

The net rates of change (R_j) of the concentrations of the three species (H⁺, HCO₃⁻, and CO₃²⁻) involved in the second dissociation step—Reaction (11)—can be described similarly. All the chemical reaction terms can be conveniently grouped by using a matrix form as:

$$\begin{bmatrix} R_{\text{H}_2\text{CO}_3} \\ R_{\text{H}^+} \\ R_{\text{HCO}_3^-} \\ R_{\text{CO}_3^{2-}} \end{bmatrix} = \begin{bmatrix} -1 & 0 \\ 1 & 1 \\ 1 & -1 \\ 0 & 1 \end{bmatrix} \begin{bmatrix} (k_{f,ca}c_{\text{H}_2\text{CO}_3} - k_{b,ca}c_{\text{H}^+}c_{\text{HCO}_3^-}) \\ (k_{f,bi}c_{\text{HCO}_3^-} - k_{b,bi}c_{\text{H}^+}c_{\text{CO}_3^{2-}}) \end{bmatrix} \quad (14)$$

At equilibrium, all the net rates, R_j , are equal to zero. Generally, for any set of k chemical reactions involving j species, one can write compactly:

$$R_j = a_{jk}r_k \quad (15)$$

where tensor notation applies for the subscripts, a_{jk} is the stoichiometric matrix where row j represents the j -th species, column k represents the k -th chemical reaction, and r_k is the reaction rate vector. Using this technique, any number of homogenous chemical reactions can be added to the model with little effort. This chemical reaction model does not prescribe a priori whether any particular reaction will be locally or globally in equilibrium, as is often done. If the homogenous chemical reaction rates, k_f and k_b , for a particular reaction are very large, the net reaction

TABLE 2
Equilibrium (K), Forward (k_f), and Backward (k_b) Reaction Rate Coefficients (Note: $K = k_f/k_b$)

Constant	Source
$K_{\text{sol}} = \frac{14.5}{1.00258} \times 10^{-(2.27+5.65 \times 10^{-3} T_f - 8.06 \times 10^{-6} T_f^2 + 0.075 \times I)}$ molar/bar	Oddo and Tomson ³⁸
$K_{\text{H}_2\text{S, sol}} = 10^{-0.71742672 - 0.012145427 \times T_c + 5.6659982 \times 10^{-5} \times T_c^2 - 8.1902716 \times 10^{-8} \times T_c^3}$ molar/bar	IUPAC data ³⁹
$K_{\text{wa}} = 10^{-(29.3868 - 0.0737549 \times T_K + 7.47881 \times 10^{-5} \times T_K^2)}$ molar ²	Kharaka, et al. ⁴⁰
$k_{\text{b, wa}} = 7.85 \times 10^{10} \text{ M}^{-1} \text{ s}^{-1}$	Delahay ²⁸
$K_{\text{hy}} = 2.58 \times 10^{-3}$	Palmer and van Eldik ⁴¹
$k_{\text{f, hy}} = 10^{329.85 - 110.541 \times \log T_K - \frac{17.265.4}{T_K}}$ s ⁻¹	Palmer and van Eldik ⁴¹
$K_{\text{ca}} = 387.6 \times 10^{-(6.41 - 1.594 \times 10^{-3} T_f + 8.52 \times 10^{-6} T_f^2 - 3.07 \times 10^{-5} p - 0.4772 \times I^{1/2} + 0.1180 \times I)}$ molar	Oddo and Tomson ³⁸
$K_{\text{f, ca}} = 10^{5.71 + 0.0526 \times T_C - 2.94 \times 10^{-4} \times T_C^2 + 7.91 \times 10^{-7} \times T_C^3}$ s ⁻¹	Comprehensive Chemical Kinetics ⁴²
$K_{\text{bi}} = 10^{-(10.61 - 4.97 \times 10^{-3} T_f + 1.331 \times 10^{-5} T_f^2 - 2.624 \times 10^{-5} p - 1.166 \times I^{1/2} + 0.3466 \times I)}$ molar	Oddo and Tomson ³⁸
$k_{\text{f, bi}} = 10^9 \text{ s}^{-1}$	Estimated
$K_{\text{H}_2\text{S}} = 10^{-(15.345 - 0.045676 \times T_K + 5.9666 \times 10^{-5} \times T_K^2)}$ molar	Kharaka, et al. ⁴⁰
$k_{\text{f, H}_2\text{S}} = 10^4 \text{ s}^{-1}$	Estimated
$K_{\text{HS}^-} = 10^{-(23.93 - 0.030446 \times T_K + 2.4831 \times 10^{-5} \times T_K^2)}$ molar	Kharaka, et al. ⁴⁰
$k_{\text{f, HS}^-} = 1 \text{ s}^{-1}$	Estimated
$K_{\text{HAC}} = 10^{-(6.66104 - 0.0134916 \times T_K + 2.37856 \times 10^{-5} \times T_K^2)}$ molar	Kharaka, et al. ⁴⁰
$k_{\text{f, HAC}} = 3.2 \times 10^5 \text{ s}^{-1}$	Vetter ⁴³
$K_{\text{HSO}_4^-} = 10^{1.54883 - 0.00998 \times T_K - 5.9254 \times 10^{-6} \times T_K^2}$ molar	Kharaka, et al. ⁴⁰
$k_{\text{f, HSO}_4^-} = 1 \text{ s}^{-1}$	Estimated

Note: In the table, T_f is temperature in degrees Fahrenheit, T is absolute temperature in Kelvin, T_c is temperature in degrees Celsius, I is ionic strength in molar, and p is the pressure in psi.

term, R_j , will be much larger than the other terms in transport equations below (Equation [20]), reducing it to $R_j = 0$, what is a condition of equilibrium. This means that the concentrations of the species involved will be at equilibrium, irrespective of other processes (diffusion, migration, etc.). In the case of slow chemical reactions the concentrations of species will be determined by other terms in transport Equation (20), resulting in a nonequilibrium concentration field. The equilibrium, forward, and backward reaction rate coefficients for reactions included in the present model, defined in Table 1, are listed in Table 2.

One heterogeneous chemical reaction of particular interest is the FeCO_3 precipitation/dissolution reaction. When the concentration of Fe^{2+} and CO_3^{2-} species locally exceeds the solubility limit (i.e., the ionic product, $c_{\text{Fe}^{2+}} c_{\text{CO}_3^{2-}}$, is larger than the solubility limit, K_{sp}), conditions are met for precipitation. However, for ionic products only slightly more than the

solubility limit and at low temperatures, the precipitation rate is so low that very little film is formed. Typically, to get appreciable rates of film formation, high temperature ($>60^\circ\text{C}$) and considerable supersaturation ($S = c_{\text{Fe}^{2+}} c_{\text{CO}_3^{2-}} / K_{\text{sp}}$) are required.

Nucleation of crystalline films is a very difficult process to model mathematically. In addition, in many corrosion situations the rate of precipitation is believed to be controlled by the crystal growth rate rather than nucleation rate. In the case of FeCO_3 precipitation, two studies⁴⁴⁻⁴⁵ have proposed somewhat different expressions for the precipitation (crystal growth) rate, and both have been tested in the present model:

According to Johnson and Tomson:⁴⁴

$$R_{\text{FeCO}_3} = A \times e^{54.8 - \frac{123.0 \text{ kJ/mol}}{RT}} \times K_{\text{sp}} \times (S^{1/2} - 1)^2 \quad (16)$$

TABLE 3

Electrochemical Parameters for the Reactions Included in the Model That Fit the General Rate Equation (18),

Where the Exchange Current Density is: $i_o = i_{oref} \left(\frac{C_{H^+}}{C_{H^+ref}} \right)^{a_1} \left(\frac{C_{CO_2}}{C_{CO_2ref}} \right)^{a_2} \left(\frac{C_{H_2CO_3}}{C_{H_2CO_3ref}} \right)^{a_3} \times e^{-\frac{\Delta H}{R} \left(\frac{1}{T} - \frac{1}{T_{ref}} \right)}$

	i_{oref} A m ²	a_1	C_{H^+ref} molar	a_2	C_{CO_2ref} molar	a_3	$C_{H_2CO_3ref}$ molar	$\frac{\Delta H}{R}$ kJ mol	T_{ref} °C	E_{rev} V	b V
$2H^+ + 2e^- \rightarrow H_2$	0.05	0.5	10^{-4}	0	N/A	0	N/A	30	25	$-\frac{2.3RT}{F} \text{pH}$	$\frac{2.3RT}{2F}$
$2H_2CO_3 + 2e^- \rightarrow H_2 + 2HCO_3^-$	0.06	-0.5	10^{-5}	0	N/A	1	10^{-4}	50	20	$-\frac{2.3RT}{F} \text{pH}$	$\frac{2.3RT}{2F}$
$Fe \rightarrow Fe^{2+} + 2e^-$	1	1 for $p_{CO_2} < 1$ bar 0 for $p_{CO_2} = 1$ bar	10^{-4}	2 for $\text{pH} < 4$ 1 for $4 < \text{pH} < 5$ 0 for $\text{pH} > 5$	0.0366	0	N/A	37.5	25	-0.488	0.03 for $\text{pH} < 4$ 0.08 for $4 < \text{pH} < 5$ 0.12 for $\text{pH} > 5$

Note: ΔH is activation energy and T_{ref} is the reference temperature. Data and mechanisms were taken from Reference 29 for the cathodic reaction and Reference 34 for the anodic reaction.

According to van Hunnik, et al.:⁴⁵

$$R_{FeCO_3} = A \times e^{52.4 - \frac{119.8 \text{ kJ/mol}}{RT}} \times K_{sp} \times (S - 1)(1 - S^{-1}) \quad (17)$$

In these two expressions, A is the surface area available for precipitation per unit volume and K_{sp} is the precipitation rate constant. According to the present model, $FeCO_3$ precipitation can occur on the steel surface or within the pores of a given porous surface film. In the porous film, A is equal to the surface area of the pores per unit volume. For $FeCO_3$ films it is hard to find values for A in the literature. Instead, a value was used based on a simple calculation for a model film consisting of spherical particles with a radius of 1 μm to 10 μm placed in a lattice with a distance of 1 μm to 10 μm from particle to particle, giving $A \approx 10^5 \text{ m}^{-1}$. The solubility product (K_{sp}) for $FeCO_3$ is modeled as a function of temperature ($^\circ\text{C}$) and ionic strength based on the IUPAC data⁴¹ and in-house calculations (Thermo-Calc[†] program).⁴⁶

Repeated observations were made that crystals usually dissolve much faster than they grow: a factor of 5 is not uncommon.⁴⁷ In most cases, it can be assumed that the rate of dissolution is controlled by the rate of mass transfer of the solvated species from the surface of the crystal into the bulk solution.⁴⁷ In the present version of the model, dissolution is not included.

$FeCO_3$ precipitation has been implemented in the model as a chemical reaction taking place at the steel surface, in the porous corrosion film and on the film surface. The precipitation reaction acts as a sink for Fe^{2+} and CO_3^{2-} ions, influencing the fluxes and con-

centration gradients for both the ions and all other carbonic species.

Electrochemical Reactions at the Steel Surface

In the first approximation, the rates of the electrochemical reactions at the metal surface depend on the electrical potential of the surface, the surface concentrations of species involved in those reactions and temperature. Since electrochemical reactions involve exchange of electrons, the reaction rate can be conveniently expressed as a rate at which the electrons are "consumed or released" (i.e., in terms of an electrical current density, i). Fundamental rate equations of electrochemistry relate i to the potential at the metal surface (E), via an exponential relationship:

$$i = \pm i_o \times 10^{\pm \frac{E - E_{rev}}{b}} \quad (18)$$

which can be written down for each of the electrochemical reactions involved in a corrosion process such as Reactions (5), (6), and (9). The positive sign applies for anodic reactions such as Reaction (9) while the negative sign applies for cathodic reactions such as Reactions (5) through (8). In Equation (18), i_o is the exchange current density, E_{rev} is the reversible potential, while b is the Tafel slope, all characteristic for a particular electrochemical reaction. In most cases, i_o and E_{rev} are nonlinear functions of the surface concentration of species involved in a particular reaction, while all three parameters are functions of temperature. A summary about how these parameters are calculated is given in Table 3, while the details are described elsewhere (Nesic and coworkers describe the cathodic reaction²⁹ and the anodic reaction³⁴).

[†] Trade name.

For a spontaneous corrosion process, the unknown electrical potential at the metal surface, E (also called corrosion potential and open-circuit potential) can be found from the charge balance equation at the metal surface:

$$\sum_1^{n_a} i_a = \sum_1^{n_c} i_c \quad (19)$$

where n_a and n_c are the total number of anodic and cathodic reactions, respectively. In situations where external polarization is applied (e.g., during potentiodynamic experiments, cathodic protection using "impressed" current or in electrochemical reactors), the potential, E , is known explicitly.

Transport Processes

Species conservation equations are used to describe the transport of all the species in the solution, irrespective of whether they are involved in the electrochemical reactions at the metal surface or in the homogenous chemical reactions. A full list of species accounted for in the present version of the model, along with their diffusion coefficients, is shown in Table 4. Since this is a model of uniform corrosion, a one-dimensional computational domain is sufficient, stretching from the steel surface through the pores of a surface film and the mass-transfer boundary layer, ending in the bulk of the solution, as sketched in Figure 1. The flow field is assumed to be turbulent in the bulk solution so that the transport of species on that side of the boundary layer is dominated by turbulent mixing, while in the sublayer closer to the surface and in the pores of the surface film it is controlled by molecular transport (diffusion). Quite different transport rates are typically found in these three regions, large in the turbulent boundary layer, intermediate in the molecular diffusion-dominated boundary layer, and low in the porous film.

For the domain between the two boundaries, the concentration of each species is governed by a species conservation (mass balance) equation. The equation that describes transport for species (i) in the presence of chemical reactions, which is valid for the liquid boundary layer³⁷ and the porous film,⁵⁰ is:

$$\underbrace{\frac{\partial \epsilon c_j}{\partial t}}_{\text{accumulation}} = - \underbrace{\frac{\partial (\kappa N_j)}{\partial x}}_{\text{net flux}} + \underbrace{\epsilon R_j}_{\text{source or sink due to chemical reactions}} \quad (20)$$

where c_j is the concentration of species j ; ϵ and κ are the volumetric porosity and the surface permeability of the film, respectively (both equal to one outside the film—in the boundary layer); N_j is the flux of species j ; R_j is the source or sink of species j due to all the chemical reactions in which the particular species is involved; t is time; and x is the spatial coordinate.

TABLE 4

Species Accounted for in the Present Version of the Model and the Corresponding Reference Molecular Diffusion Coefficient

Species	Diffusion Coefficient (m ² /s)	Source
CO ₂	1.96 × 10 ⁻⁹	Perry ⁴⁸
H ₂ CO ₃	2.00 × 10 ⁻⁹	Kvarekvål ⁴⁹
HCO ₃ ⁻	1.105 × 10 ⁻⁹	Newman ³⁷
CO ₃ ²⁻	0.92 × 10 ⁻⁹	Kvarekvål ⁴⁹
H ⁺	9.312 × 10 ⁻⁹	Newman ³⁷
OH ⁻	5.26 × 10 ⁻⁹	Newman ³⁷
Fe ²⁺	0.72 × 10 ⁻⁹	Kvarekvål ⁴⁹
Cl ⁻	2.032 × 10 ⁻⁹	Newman ³⁷
Na ⁺	1.334 × 10 ⁻⁹	Newman ³⁷
Ca ²⁺	0.792 × 10 ⁻⁹	Newman ³⁷
Ba ²⁺	0.847 × 10 ⁻⁹	Newman ³⁷
Si ²⁺	0.791 × 10 ⁻⁹	Newman ³⁷
HAc	1.24 × 10 ⁻⁹	Perry ⁴⁸
Ac ⁻	1.089 × 10 ⁻⁹	Newman ³⁷
H ₂ S	1.61 × 10 ⁻⁹	Perry ⁴⁸
HS ⁻	2.00 × 10 ⁻⁹	Estimated
S ²⁻	2.00 × 10 ⁻⁹	Estimated
HSO ₄ ⁻	1.33 × 10 ⁻⁹	Newman ³⁷
SO ₄ ²⁻	1.065 × 10 ⁻⁹	Newman ³⁷

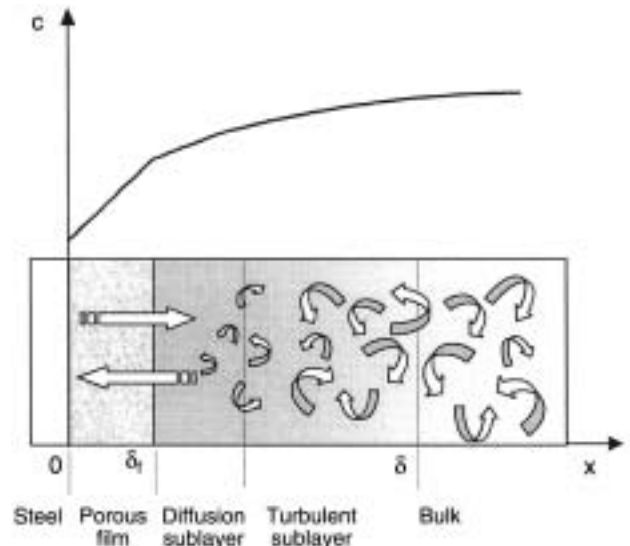


FIGURE 1. Sketch of the calculation domain: δ_f is the surface film thickness; $\delta - \delta_f$ is the liquid boundary layer thickness. The curve on the top represents a typical variation of a single species concentration expected from theory.

Means of computing R_j have been described. The flux of species N_j in Equation (20) has three components: diffusion, migration, and convection:

$$N_j = \underbrace{-D_j \frac{\partial c_j}{\partial x}}_{\text{diffusion}} - \underbrace{z_j u_j F c_j \frac{\partial \phi}{\partial x}}_{\text{migration}} + \underbrace{c_j v}_{\text{convection}} \quad (21)$$

where D_j is the molecular diffusion coefficient of species j , z_j is the electrical charge of species j , u_j is the

TABLE 5
Liquid Properties as a Function of Temperature^(A)

Dynamic viscosity	$\mu = 0.001002 \times 10^{\frac{1.3277 \times (293.15 - T) - 0.001053 \times (298.15 - T)^2}{T - 168.15}}$ kg/ms
Density	$\rho = (753.596 + 1.87748 \times T - 0.003564 \times T^2)$ kg/m ³
Dielectric constant	$\xi = \frac{10^{-9}}{36\pi} \times (249.21 - 0.79069 \times T + 0.00072997 \times T^2)$
Diffusion coefficient (subscript _{ref} denotes reference values, see Table 4)	$D_i = D_{ref} \frac{T}{T_{ref}} \frac{\mu_{ref}}{\mu}$

^(A) Source: CRC Handbook of Chemistry and Physics.⁵²

mobility of species *j*, *F* is the Faradays constant, and ϕ is the electric potential in the solution.

The instantaneous velocity (*v*) appearing in the convection term is not known explicitly in turbulent flow unless results of full DNS⁽¹⁾ simulation are available. A well-established statistical technique is to divide the instantaneous velocity into a time-averaged and a turbulent-fluctuating component. Close to a solid surface, the former is parallel to the surface and does not contribute to the transport of species in the direction normal to the metal surface. The turbulent convection term in Equation (21), $c_j v$ arising from the presence of eddies, can be approximated by a "turbulent diffusivity" term,⁵¹ $-D_t \frac{\partial c_j}{\partial x}$. The turbulent diffusion coefficient (*D_t*) is a function of the distance from the metal or film surface and is given by:⁵¹

$$D_t = \begin{cases} 0 & \text{for } x < \delta_f \\ 0.18 \left(\frac{x - \delta_f}{\delta - \delta_f} \right)^3 \frac{\mu}{\rho} & \text{for } x > \delta_f \end{cases} \quad (22)$$

The liquid boundary layer thickness is typically a function of the Reynolds number. For pipe flow, it reads:⁵¹

$$\delta - \delta_f = 25 \text{Re}^{-7/8} d \quad (23)$$

where *d* is the hydraulic diameter, $\text{Re} = \rho U d / \mu$ is the Reynolds number, *U* is bulk velocity, ρ is the density, and μ is dynamic viscosity. The density and viscosity are modeled as a function of temperature as shown in Table 5. It is assumed that there is no fluid flow within the porous film (for $x < \delta_f$).

Not all terms in Equations (20) and (21) are easily found. The molecular diffusion coefficients, *D_j*, for various species are readily listed in the open literature (the ones used in this study are listed in Table 4). The mobility (*u_j*) can best be determined via its

relationship with the diffusion coefficient via the Nernst-Einstein equation:³⁷

$$D_j = RTu_j \quad (24)$$

In the first approximation, the permeability (κ) of surface films for transport of species in Equation (20) depends on the amount of pores in the film (expressed as superficial porosity, ϵ_s , in a plane parallel to the metal surface) and the shape and connections between the pores (expressed via the tortuosity, ψ):

$$\kappa = \psi \epsilon_s \quad (25)$$

If one assumes that superficial porosity (ϵ_s) is approximately equal to volumetric porosity (ϵ) and that tortuosity is proportional to a square root of porosity (in an analogy with the theory of porous electrodes³⁷), permeability of surface films for transport of species κ can be found as:

$$\kappa = \epsilon^{3/2} \quad (26)$$

The electric potential gradient ($\partial\phi/\partial x$) in Equation (21) can be found via:³⁷

$$\frac{\partial}{\partial x} \left(\kappa \xi \frac{\partial \phi}{\partial x} \right) = -\epsilon F \sum_j z_j c_j \quad (27)$$

where ξ is the dielectric constant and depends on temperature as indicated in Table 5. It is clear from Equation (27) that the electrical potential field ($\partial\phi/\partial x$) in the solution is established due to the charge imbalance ($\sum_j z_j c_j$). In the present model, a local charge imbalance is established as a result of species concentration gradients and different diffusion coefficients of charged species in solution. The proportionality constant ($\epsilon F / \kappa \xi$) in Equation (27) is so large that even a tiny separation of charge results in an appreciable potential gradient, which in practice prevents any further significant separation of charge. Often, instead of Equation (27), a simple electroneutrality equation is used:³⁷

⁽¹⁾ DNS stands for Direct Numerical Simulation of the Navier Stokes equations. This computational method resolves turbulent flow fields completely in time and space. However, due to very large computational efforts involved, DNS is applicable only to very simple flow geometries and low Reynolds numbers.

$$\sum_j z_j c_j = 0 \quad (28)$$

This equation is based on an assumption that any amount of solution, however small, is always electroneutral (i.e., there is a perfect balance between the positively and negatively charged species everywhere in the solution). In other words, no charge separation can occur. The electroneutrality Equation (28) appears to be simpler than Equation (27), however, it does not offer an explicit way to compute the electrical potential gradient ($\partial\phi/\partial x$) needed to determine the contribution of migration in the transport Equation (21). A way around this problem has been suggested by Newman,³⁷ which amounts to eliminating the potential gradient from the transport equations by implicitly using the electroneutrality equation. However, the consequence is that all the charged species become explicitly linked in the transport equation through a complex nonlinear migration term. To avoid this problem in this study, the linear equation for the electric potential (Equation [27]) has been used to explicitly compute the electrical potential gradient ($\partial\phi/\partial x$) without invoking the electro-neutral condition (Equation [28]).

Initial and Boundary Conditions

Uniform concentrations of species in chemical equilibrium are used as initial conditions for all the species.

These equilibrium concentrations are also used as boundary conditions in the bulk where it is assumed that all species are thoroughly mixed by turbulence.

At the metal surface, zero flux, $N_j = 0$, is specified for the species not involved in the electrochemical equation. For species j involved in electrochemical reactions at the metal surface, the flux at the metal surface can be determined from:

$$N_j = -\frac{i_j}{n_j F} \quad (29)$$

The partial current (i_j) for a given species is easily obtained from Equation (18) once the corrosion potential (E) is known; n_j is the number of mols of electrons exchanged per mol of species j participating in a particular electrochemical reaction. For example, $n_{H^+} = 1 \text{ mol}_e/\text{mol}_{H^+}$ for Reaction (5).

The electric potential (ϕ) in the solution, appearing in Equation (27), is given a constant (reference) value (ϕ_{ref}) in the first node adjacent the steel surface. In the bulk, a potential gradient can be specified (derived from zero total current condition³⁷) as:

$$\xi \frac{d\phi}{dx} \Big|_b = -\frac{\xi F}{\kappa_c} \sum_j z_j (D_j + D_t) \frac{dc_j}{dx} \Big|_b \quad (30)$$

where:

$$\kappa_c = F^2 \sum_j z_j^2 u_j c_j \Big|_b \quad (31)$$

Since the concentrations c_j are known in the bulk (they are specified via boundary conditions as equilibrium), κ_c can be directly computed, and the boundary condition (Equation [30]) is linear.

Growth of Iron Carbonate Films

In the model described, the means of calculating the thickness of FeCO_3 film (δ_j) and its porosity (ϵ) are not given. While the rate of FeCO_3 precipitation can be readily calculated from Equations (16) or (17), it is not straightforward to compute the morphology and thickness of the resulting solid film precipitate. At this stage, buildup of corrosion films as a function of time due to FeCO_3 precipitation is not included in the model. If corrosion in the presence of corrosion product films is to be calculated, the user has to specify the thickness and porosity of the film.

On the other hand, the model can be used to predict the equivalent of a scaling tendency as proposed by van Hunnik, et al.,⁴⁵ which is a ratio between the precipitation rate and the corrosion rate before any film is formed.

NUMERICAL METHOD

All the relevant equations have been listed. To summarize, for n species in the solution, one has $n+1$ equations; that is, one transport Equation (20) for each species and Equation (27) for the potential. Since all the equations are strongly and nonlinearly coupled through the chemical reaction and migration terms, they all have to be solved simultaneously, together with the boundary conditions including the nonlinear surface charge balance, Equation (19).

The differential transport equations (Equation [20]) were discretized using a finite difference method and a nonuniform grid as sketched in Figure 2. For example, the finite difference approximation of the transport equations (Equation [20]) for species j in control volume p is given by:

$$\epsilon_p \frac{C_{j,p}^{n+1} - C_{j,p}^n}{\Delta t} \Delta x_p = -\kappa_{p+1/2} N_{j,p+1/2}^{n+1} + \kappa_{p-1/2} N_{j,p-1/2}^{n+1} + \epsilon_p R_{j,p}^{n+1} \Delta x_p \quad (32)$$

Superscripts $n+1$ and n denote new and old points in time, respectively; Δx_p is the size of the control volume p . A fully implicit time discretization scheme is used here for stability reasons where all the variables on the right-hand side of Equation (32) are taken at the new time, $n+1$. Following spatial discretization, all the terms are evaluated in the center of the con-

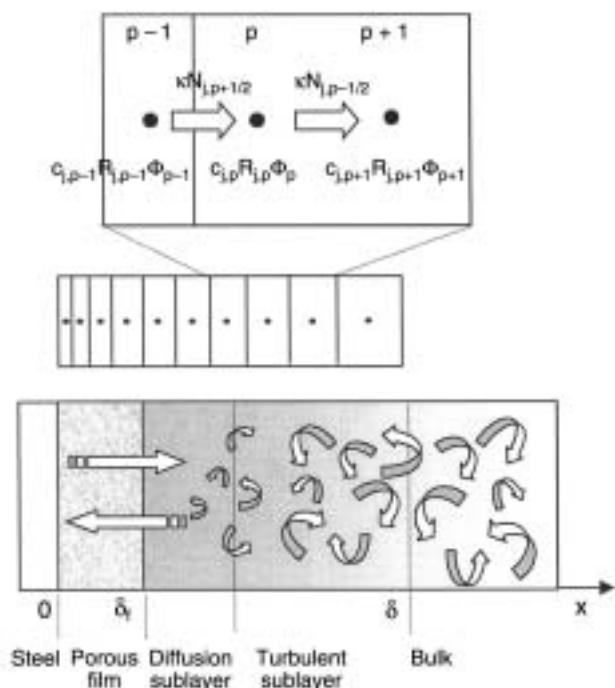


FIGURE 2. Sketch of the computational grid and the control volumes used for discretization of the computational domain. The concentrations, the potential, and the chemical reaction terms are all computed in the center of the control volume, while the fluxes are computed on the interfaces.

control volumes, except the fluxes, which are evaluated at the control volume boundaries (Figure 2). Harmonic averaging is used to calculate these fluxes based on values of the variables in the node points $p-1$, p , and $p+1$ on each side of the boundaries. When there is an abrupt change in permeability (e.g., at the interface between the fluid and the film), other interpolation schemes would not be conservative and would lead to large numerical errors. All the nonlinear terms—the fluxes, the chemical reaction rate terms, and all the terms in the surface charge balance equation—are linearized in variable space. This is achieved by using Taylor series expansion around the known solution and by keeping only the constant and the linear term. For example, in the case of the chemical reaction terms, this reads:

$$R_{j,p}^{n+1} = a_{jk} r_k^{n+1} = a_{jk} \left[r_k^{n'} + \frac{\partial r_k^{n'}}{\partial c_j} (c_{j,p}^{n+1} - c_{j,p}^{n'}) \right] \quad (33)$$

where superscript n' denotes the known solution. To avoid instabilities, an iterative process is applied where the n' -solution is gradually changed from the old time solution (n) to the new time solution ($n+1$) at the end of the iterations. The discretization procedure described above converts the set of nonlinear partial differential equations for species transport (Equation [20]) and the electric potential (Equation [27]) into a

set of linear equations in the form $Ax = b$. The matrix A is block tri-diagonal. In the present study, the equations are solved directly by a LU solver.⁵³

The model was implemented in Fortran programming language to increase the speed of the lengthy calculations.

A typical hydrodynamic boundary layer thickness in turbulent pipe flow is on the order of $100 \mu\text{m}$ to $1,000 \mu\text{m}$, while the corresponding mass-transfer boundary layer is thinner, approximately by an order of magnitude due to the large Sc numbers of the species involved ($Sc \sim 10^2$ to 10^3). Therefore, the one-dimensional spatial grid (depicted in Figures 1 and 2) needed to cover typically $10 \mu\text{m}$ to $300 \mu\text{m}$ in various simulations. To successfully resolve the concentration profiles in the mass-transfer boundary layer, typically 25 to 100 spatial nodes were used. Grid refinement was used regularly to establish grid independence of the final solution.

In uniform corrosion without film formation, a stable corrosion rate (steady state) is achieved rather fast as the relaxation time of the mass-transfer boundary layer is on the order of 0.1 s to 1 s. Therefore, if one is only interested in the steady state, the choice of the time step is not crucial for the final result. However, problems arise in the beginning of the simulation ($t = 0$) due to the abrupt initiation of corrosion and introduction of large species fluxes at the metal surface. To start the simulation without numerical instabilities, very small time steps had to be used (10^{-3} s to 10^{-2} s) combined with significant underrelaxation (0.1 to 0.2) of the fluxes.

VERIFICATION—COMPARISON WITH EXPERIMENTS

Any model cannot be trusted before its performance is compared with experimental values. A number of such comparisons with laboratory data are presented below.

Potentiodynamic Sweep Measurements

One way to thoroughly test a mechanistic corrosion model is to try to simulate a standard laboratory corrosion experiment such as a potentiodynamic sweep as it carries a wealth of information about the various processes underlying corrosion. To achieve this goal, the original model was adapted so that the simulation was executed much in the same way as an experimental potentiodynamic sweep is done: a steady-state corrosion potential/current was calculated first and then the potential was “swept” anodically and cathodically. This was achieved by excluding the surface charge balance Equation (19) from the calculations. Instead, the surface potential was specified explicitly and changed at a slow rate so that equilibrium concentrations were reached at each point. In the actual experiments, which were con-

ducted under strictly controlled chemical, electrochemical, and hydrodynamic conditions, two different flow geometries were studied simultaneously in the same electrolyte within a glass loop: a rotating cylinder and pipe flow.⁵⁴

As indicated in Figures 3 and 4, the agreement between the model predictions and the experiments is very good. The cathodic branch of the curve exhibits a limiting current, which is a direct consequence of depletion of H^+ ions near the surface and the slow hydration rate of CO_2 . This was an important test for the transport model since all the electrochemical reaction rates depend on surface concentrations and no explicit limiting current equations were built into the model. It should be noted that almost identical total cathodic limiting currents were obtained, irrespective of whether the direct reduction of H_2CO_3 Reaction (6) was included in the model (Figure 4) or not (Figure 3). This confirms the well-known fact that it is very hard to distinguish the two mechanisms for hydrogen evolution, both computationally and experimentally. The underlying anodic and cathodic reactions suggest that under these conditions the corrosion rate is predominantly under charge-transfer control. This is impossible to deduce by looking at the potentiodynamic sweep curve alone. Discrepancies between the predicted and the experimental sweep increase at very negative potentials. This is caused by an additional electrochemical reaction (water reduction), which occurs at very negative potentials and is not presently included in the model.

Corrosion Rate Measurements

The present model was used to simulate a large number of selected flow loop corrosion experiments performed under conditions giving little or no protective film formation.⁵⁵ The experiments were performed at 20°C to 90°C, with the majority in the 40°C to 60°C range. The CO_2 partial pressure (p_{CO_2}) was between 0.3 bar and 12 bar and the flow velocity between 0.1 m/s and 13 m/s. Low pH values in the range from 3.5 to 4.5 were used, except for a few experiments at 20°C with pH ~5.5. At these conditions very high corrosion rates are obtained. The agreement between the predictions and the experiments is only modest with the model generally underpredicting the corrosion rate, as seen in Figure 5. The reason is that in these long duration experiments conducting iron carbide films formed, which increased the corrosion rate probably via a galvanic effect,⁵⁵⁻⁵⁶ a phenomenon not presently included in the model. In addition, a careful analysis has revealed that for the experiments conducted at high velocity, low temperatures, and low partial pressures of CO_2 , the agreement is better (Figure 6). It can be speculated that at these high flow rates the loose iron carbide films were removed. More importantly, most of the experimentally determined coefficients

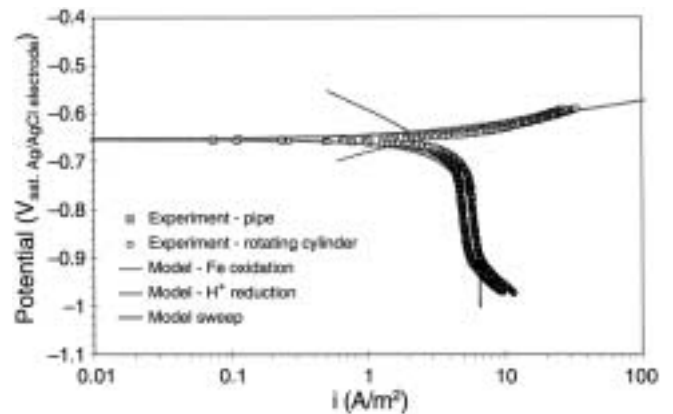


FIGURE 3. Comparison between predicted and measured potentiodynamic sweep for the case of CO_2 corrosion of carbon steel (experimental data taken from Nescic, et al.⁵⁴): 20°C, velocity = 2 m/s, pH 4, p_{CO_2} = 1 bar. Direct reduction of H_2CO_3 is disregarded.

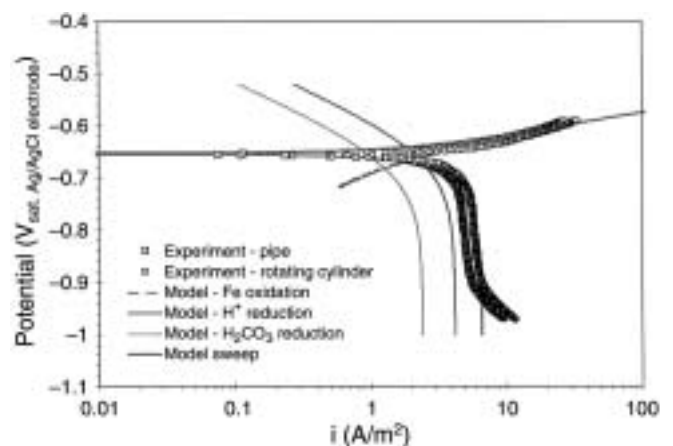


FIGURE 4. Comparison between predicted and measured potentiodynamic sweep for the case of CO_2 corrosion of carbon steel (experimental data taken from Nescic, et al.⁵⁴): 20°C, velocity = 2 m/s, pH 4, p_{CO_2} = 1 bar. Direct reduction of H_2CO_3 is included.

built into the present model were obtained at low temperatures and CO_2 partial pressures, while theoretical relationships were typically used to extend their validity to the higher temperature and pressure ranges. Clearly, this aspect of the model needs further improvement based on the input from high-temperature, high-pressure laboratory experiments.

CO_2 CORROSION NUMERICAL EXPERIMENTS

The capabilities of the present model go far beyond a mere prediction of a steady-state CO_2 corrosion rate. It can be used as a framework where different assumptions can be tested and compared to existing empirical evidence. A theoretical model such as the present one can be seen as a “numerical experiment” (i.e., an environment in which different events can be switched on/off, processes acceler-

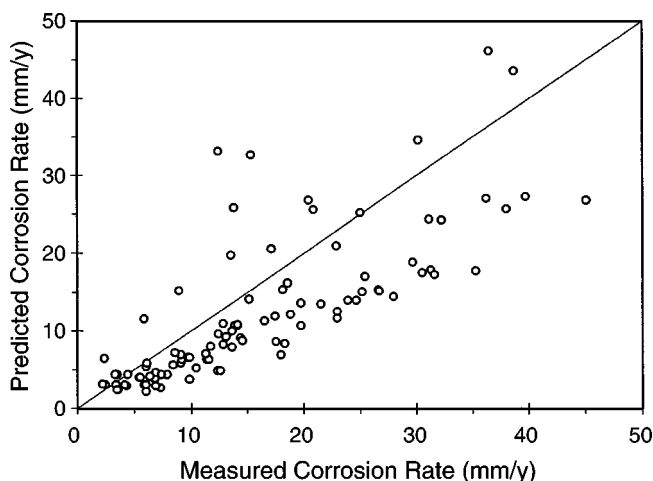


FIGURE 5. Comparison between predicted and measured corrosion rates in long duration flow loop corrosion experiments without protective films (experimental data taken from Dugstad, et al.⁵⁵): 20°C to 90°C, 0.1 m/s to 13 m/s, p_{CO_2} = 0.3 bar to 12 bar, and pH 3.5 to 6.

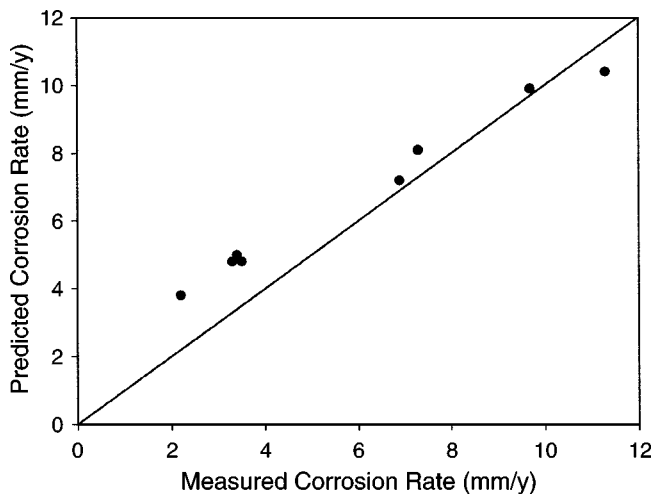


FIGURE 6. Comparison between predicted and measured corrosion rates in long duration flow loop corrosion experiments without protective films (experimental data taken from Dugstad, et al.⁵⁵): 20°C, 13 m/s, p_{CO_2} = 0.3 bar to 2 bar, and pH 3.5 to 6.

ated/decelerated, at will—an impossible task in a real experiment). In addition, the numerical experiment can be used to investigate the underlying processes governing the corrosion process for a given set of conditions. To illustrate this aspect of the model, simulations were made with and without any CO_2 gas dissolved in the water and $t = 20^\circ\text{C}$, pipe diameter = 0.1 m, flow velocity = 1 m/s, and pH 6. It is known from practice that in deaerated, nearly-neutral conditions without any CO_2 gas dissolved in the water at low temperature, the corrosion rate of mild steel is low. The present model predicts 0.01 mm/y for this situation. When CO_2 gas is introduced with a partial pressure, $p_{\text{CO}_2} = 1$ bar, and with all other parameters unchanged, the predicted corrosion rate increases to

0.27 mm/y without taking into account the direct reduction of H_2CO_3 (Equation [6]). When direct reduction of H_2CO_3 is included, the predicted corrosion rate increases further to 0.97 mm/y, which is close to experimentally observed values. This shows that an important effect of H_2CO_3 in the solution is to provide an additional source of H^+ through dissociation. To explain the increased corrosion rate in the presence of CO_2 , it is not necessary to assume direct reduction of H_2CO_3 as an additional cathodic reaction, as originally proposed by de Waard and Milliams.¹ However, when included into the calculations, direct reduction of H_2CO_3 increases the predicted corrosion rate even further.

The concentration and flux profiles for the case described above with direct reduction of H_2CO_3 included are shown in Figures 7 and 8, respectively, as function of the distance from the metal surface. At pH 6 there is little H^+ available in the bulk, and the fluxes of CO_2 and H_2CO_3 toward the surface are much larger than the flux of H^+ (all shown as negative in Figure 8 because these species move in the negative x direction). In the vicinity of the surface, CO_2 is hydrated to H_2CO_3 , which is then consumed at the metal surface, either by direct reduction or by dissociation to H^+ , which is then reduced. The corrosion products HCO_3^- and Fe^{2+} are transported away from the metal surface (shown as positive fluxes in Figure 8).

In the presence of protective films, the corrosion rate is reduced for two reasons: diffusion of species toward and away from the surface is hindered, and the surface of the metal, where the corrosion reactions occur, is “blocked” by the attached film. The latter effect is often ignored in analysis of corrosion in the presence of surface films. Concentration profiles of the dissolved species in the solution shown in Figure 9 illustrate this. A two-layered film is assumed here with a total film thickness of 10 μm . The inner layer next to the metal surface is quite dense ($\epsilon = 0.1$) while the outer layer facing the solution is more open ($\epsilon = 0.6$). The resulting concentration profiles show that most of the resistance for diffusion is in the dense layer of the film. The resulting corrosion rate is predicted to be 0.16 mm/y, which is more than 20 times less than that obtained for the same conditions without the film.

The full capability of this model to be used as a numerical experiment is exploited in the second part of this study, where the focus is on the conditions affecting protective FeCO_3 film formation and on the role of these films in reducing CO_2 corrosion rates.

CONCLUSIONS

❖ The mechanistic model created covers most of the processes important in uniform CO_2 corrosion: electrochemical reactions at the steel surface, diffu-

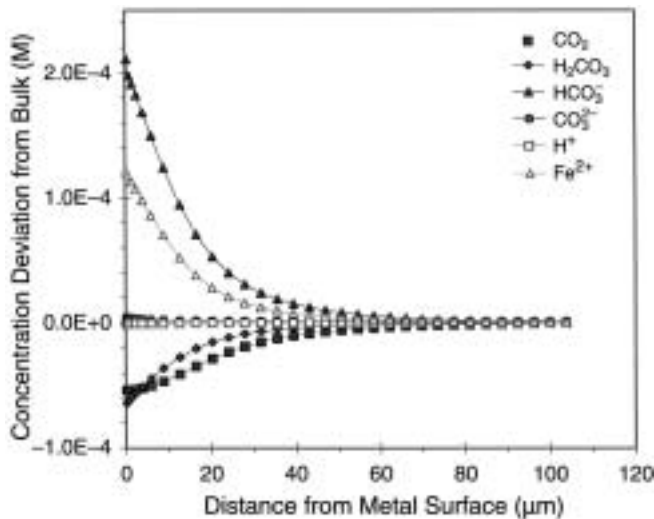


FIGURE 7. Deviation of dissolved species concentrations from the bulk values as a function of distance from the steel surface: 20°C, pipe diameter = 0.1 m, flow velocity = 1 m/s and pH 6, and p_{CO_2} = 1 bar.

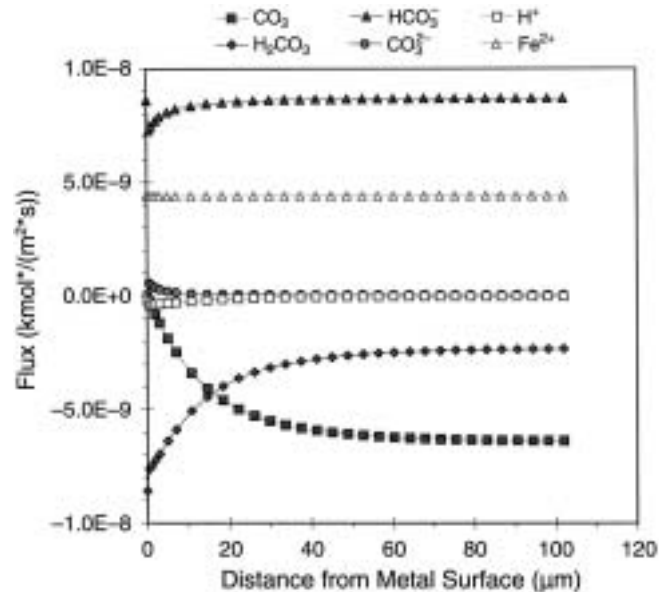


FIGURE 8. Flux of dissolved species as a function of distance from the steel surface: 20°C, pipe diameter = 0.1 m, flow velocity = 1 m/s and pH 6, and p_{CO_2} = 1 bar.

sion of species to and from the bulk including diffusion through porous surface films, migration as a result of the establishment of potential gradients, and homogenous chemical reactions including precipitation of surface films. These processes are mathematically modeled using fundamental equations. The model simulates the corrosion rate and concentration, and flux profiles for all involved species.

❖ Comparisons with laboratory experiments have revealed the strengths of the model such as its ability to assist in understanding the complex processes taking place during corrosion in the presence of surface films. However, the comparisons have also uncovered the model's weaknesses primarily related to the lack of reliable experimental data at higher temperatures and CO_2 partial pressures. Also, the effects related to the presence of conducting iron carbide surface films need to be introduced if more accurate predictions are to be obtained at lower temperatures and pH. It is recognized that the properties of protective FeCO_3 corrosion product films are crucial in predicting the actual corrosion rate at higher temperatures and pH, and that mechanistic modeling of the morphology of the corrosion films is a difficult task.

ACKNOWLEDGMENTS

The present CO_2 corrosion model was developed in the joint industry project—Kjeller Sweet Corrosion V—with the following companies as participants: Shell, Elf, Total, Conoco, Agip, Statoil, Norsk Hydro, Saga Petroleum, Amoco, and Siderca. The authors acknowledge these companies for their technical and financial support and the permission to publish the present paper.

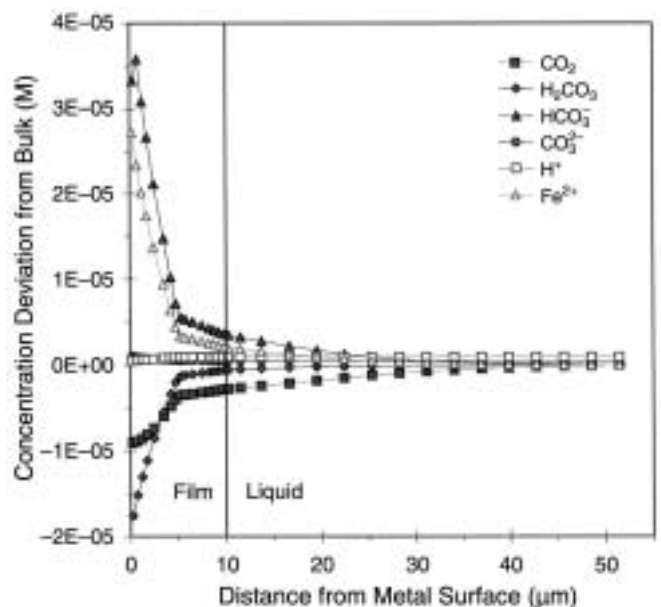


FIGURE 9. Deviation of dissolved species concentrations from bulk values as a function of distance from the steel surface; two-layered surface film 10 μm thick, porosity 0.1 next to the metal surface, and 0.6 toward the bulk solution; 80°C; pipe diameter = 0.1 m; flow velocity = 1 m/s; pH 6; and p_{CO_2} = 1 bar.

REFERENCES

1. C. de Waard, D.E. Milliams, Corrosion 31 (1975): p. 131.
2. C. de Waard, U. Lotz, D.E. Milliams, Corrosion 47 (1991): p. 976.
3. C. de Waard, U. Lotz, A. Dugstad, "Influence of Liquid Flow Velocity on CO_2 Corrosion: A Semi-Empirical Model," CORROSION/95, paper no. 128 (Houston, TX: NACE International, 1995).

4. M.R. Bonis, J.-L. Crolet, "Basics of the Prediction of the Risks of CO₂ Corrosion in Oil and Gas Wells," CORROSION/89, paper no. 466 (Houston, TX: NACE, 1989).
5. J.-L. Crolet, M.R. Bonis, SPE Prod. Eng. 6 (1991): p. 449.
6. Y.M. Gunaltun, "Combining Research and Field Data for Corrosion Rate Prediction," CORROSION/96, paper no. 27 (Houston, TX: NACE, 1996).
7. A.M.K. Halvorsen, T. Søntvedt, "CO₂ Corrosion Model for Carbon Steel Including a Wall Shear Stress Model for Multiphase Flow and Limits for Production Rate to Avoid Mesa Attack," CORROSION/99, paper no. 42 (Houston, TX: NACE, 1999).
8. "CO₂ Corrosion Rate Calculation Model," NORSOK Standard no. M-506, Norwegian Technology Standards Institution, <http://www.nts.no/norsok>, June 1998.
9. A.J. McMahon, D.M.E. Paisley, "Corrosion Prediction Modeling—A Guide to the Use of Corrosion Prediction Models for Risk Assessment in Oil and Gas Production and Transportation Facilities," Report no. ESR.96.ER.066 (Sunbury: BP International, 1997).
10. C.D. Adams, J.D. Garber, R.K. Singh, "Computer Modeling to Predict Corrosion Rates in Gas Condensate Wells Containing CO₂," CORROSION/96, paper no. 31 (Houston, TX: NACE, 1996).
11. S. Srinivasan, R.D. Kane, "Prediction of Corrosivity of CO₂/H₂S Production Environments," CORROSION/96, paper no. 11 (Houston, TX: NACE, 1996).
12. R.C. John, K.G. Jordan, S.D. Kapusta, A.L. Young, W.T. Thompson, "SweetCor: An Information System for the Analysis of Corrosion of Steels by Water and Carbon Dioxide," CORROSION/98, paper no. 20 (Houston, TX: NACE, 1998).
13. W.P. Jepson, C. Kang, M. Gopal, S. Stitzel, "Model for Sweet Corrosion in Horizontal Multiphase Slug Flow," CORROSION/97, paper no. 11 (Houston, TX: NACE, 1997).
14. R. Zhang, M. Gopal, W.P. Jepson, "Development of a Mechanistic Model for Predicting Corrosion Rate in Multiphase Oil/Water/Gas Flows," CORROSION/97, paper no. 601 (Houston, TX: NACE, 1997).
15. B.F.M. Pots, "Mechanistic Models for the Prediction of CO₂ Corrosion Rates under MultiPhase Flow Conditions," CORROSION/95, paper no. 137 (Houston, TX: NACE, 1995).
16. A. Anderko, R. Young, "Simulation of CO₂/H₂S Corrosion Using Thermodynamic and Electrochemical Models," CORROSION/99, paper no. 31 (Houston, TX: NACE, 1999).
17. E. Dayalan, F.D. de Moraes, J.R. Shadley, S.A. Shirazi, E.F. Ribicki, "CO₂ Corrosion Prediction in Pipe Flow Under FeCO₃ Scale-Forming Conditions," CORROSION/98, paper no. 51 (Houston, TX: NACE, 1998).
18. M. Sundaram, V. Raman, M.S. High, D.A. Tree, J. Wagner, "Deterministic Modeling of Corrosion in Downhole Environments," CORROSION/96, paper no. 30 (Houston, TX: NACE, 1996).
19. M.S. High, J. Wagner, S. Natarajan, "Mechanistic Modeling of Mass Transfer in the Laminar Sublayer in Downhole Systems," CORROSION/2000, paper no. 62 (Houston, TX: NACE, 2000).
20. S. Nēšić, J. Postlethwaite, M. Vrhovac, Corros. Rev. 15 (1997): p. 211.
21. R. Nyborg, "Overview of CO₂ Corrosion Models for Wells and Pipelines," CORROSION/2002, paper no. 233 (Houston, TX: NACE, 2002).
22. A. Dugstad, "Mechanism of Protective Film Formation During CO₂ Corrosion of Carbon Steel," CORROSION/98, paper no. 31 (Houston, TX: NACE, 1998).
23. R. Nyborg, "Initiation and Growth of Mesa Corrosion Attack During CO₂ Corrosion of Carbon Steel," CORROSION/98, paper no. 48 (Houston, TX: NACE, 1998).
24. R. Nyborg, A. Dugstad, "Mesa Corrosion Attack in Carbon Steel and 0.5% Chromium Steel," CORROSION/98, paper no. 29 (Houston, TX: NACE, 1998).
25. L.G.S. Gray, B.G. Anderson, M.J. Danysh, P.G. Tremaine, "Mechanisms of Carbon Steel Corrosion in Brines Containing Dissolved Carbon Dioxide," CORROSION/89, paper no. 464 (Houston, TX: NACE, 1989).
26. E. Eriksrud, T. Søntvedt, "Effect of Flow on CO₂ Corrosion Rates in Real and Synthetic Formation Waters," in Advances in CO₂ Corrosion, vol. 1, Proc. CORROSION/83 Symp. on CO₂ Corrosion in the Oil and Gas Industry, eds. R.H. Hausler, H.P. Goddard (Houston, TX: NACE, 1984), p. 20.
27. L.G.S. Gray, B.G. Anderson, M.J. Danysh, P.R. Tremaine, "Effect of pH and Temperature on the Mechanism of Carbon Steel Corrosion by Aqueous Carbon Dioxide," CORROSION/90, paper no. 40 (Houston, TX: NACE, 1990).
28. P. Delahay, J. Am. Chem. Soc. 74 (1952): p. 3,497.
29. S. Nēšić, J. Postlethwaite, S. Olsen, Corrosion 52 (1996): p. 280.
30. D.M. Drazic, "Iron and its Electrochemistry in an Active State," in Aspects of Electrochemistry, vol. 19 (New York, NY: Plenum Press, 1989), p. 79.
31. W. Lorenz, K. Heusler, "Anodic Dissolution of Iron Group Metals," in Corrosion Mechanisms, ed. F. Mansfeld (New York, NY: Marcel Dekker, 1987).
32. J.O.M. Bockris, D. Drazic, A.R. Despic, Electrochim. Acta 4 (1961): p. 325.
33. G. Schmitt, B. Rothman, Werkst. Korros. 28 (1977): p. 816.
34. S. Nēšić, N. Thevenot, J.-L. Crolet, D. Drazic, "Electrochemical Properties of Iron Dissolution in the Presence of CO₂—Basics Revisited," CORROSION/96, paper no. 3 (Houston, TX: NACE, 1996).
35. H. Davies, G.T. Burstein, Corrosion 36 (1980): p. 385.
36. K. Videm, "Fundamental Studies Aimed at Improving Models for Prediction of CO₂ Corrosion," in Progress in the Understanding and Prevention of Corrosion, Proc. 10th European Corros. Cong., vol. 1 (London, U.K.: Institute of Metals, 1993), p. 513.
37. J.S. Newman, Electrochemical Systems, 2nd ed. (Englewood Cliffs, NJ: Prentice Hall, 1991).
38. J.E. Oddo, M.B. Tomson, "Simplified Calculation of CaCO₃ Saturation at High Temperatures and Pressures in Brine Solutions," SPE of AIME (Richardson, TX: Society of Petroleum Engineers, 1982), p. 1,583.
39. IUPAC, Chemical Data Series, no. 21, "Stability Constants of Metal-Ion Complexes, Part A: Inorganic Ligands" (Pergamon Press).
40. Y.K. Kharaka, E.H. Perkins, W.D. Gunter, J.D. Debral, C.H. Bamford, "Solmineq 88: A Computer Program for Geochemical Modeling of Water Rock Interactions" (Menlo Park, CA: Alberta Research Council, 1989).
41. D.A. Palmer, R. van Eldik, Chem. Rev. 83 (1983): p. 651.
42. Comprehensive Chemical Kinetics, vol. 6 (Amsterdam, The Netherlands: Elsevier Publishing Co., 1972), p. 283-284.
43. K.J. Vetter, Electrochemische Kinetik (Berlin, Germany: Springer-Verlag, 1961), p. 406-429.
44. M.L. Johnson, M.B. Tomson, "Ferrous Carbonate Precipitation Kinetics and Its Impact on CO₂ Corrosion," CORROSION/91, paper no. 268 (Houston, TX: NACE, 1991).
45. E.W.J. van Hunnik, B.F.M. Pots, E.L.J.A. Hendriksen, "The Formation of Protective FeCO₃ Corrosion Product Layers in CO₂ Corrosion," CORROSION/96, paper no. 6 (Houston, TX: NACE, 1996).
46. B. Sundman, "Thermo-Calc Version L, Users' Guide" (Stockholm, Sweden: Dept. of Materials Science and Engineering, Royal Institute of Technology, 1997).
47. J.W. Mullin, Crystallization, 3rd ed. (Oxford, U.K.: Oxford Press, 1993).
48. R.H. Perry, D. Green, Perry's Chemical Engineers' Handbook, 50th ed. (New York, NY: McGraw-Hill, 1984).
49. J. Kvarekvål, "A Kinetic Model for Calculating Concentration Profiles and Fluxes of CO₂-Related Species Across the Nernst Diffusion Layer," CORROSION/97, paper no. 5 (Houston, TX: NACE, 1997).
50. J. Bear, Dynamics of Fluids in Porous Media (New York: Dover Publications, 1972).
51. J.T. Davies, Turbulence Phenomena (London, U.K.: Academic Press, 1972).
52. D.R. Lide, "CRC Handbook of Chemistry and Physics," 75th ed. (New York, NY: CRC Press, 1995).
53. H. Press, Numerical Recipes in FORTRAN: The Art of Scientific Computing, 2nd ed. (Cambridge, U.K.: Cambridge University Press, 1992).
54. S. Nēšić, G.Th. Solvi, S. Skjerve, Br. Corros. J. 32 (1997): p. 269.
55. A. Dugstad, L. Lunde, K. Videm, "Parametric Study of CO₂ Corrosion of Carbon Steel," CORROSION/94, paper no. 14 (Houston, TX: NACE, 1994).
56. J.-L. Crolet, N. Thevenot, S. Nēšić, "Role of Conductive Corrosion Products on the Protectiveness of Corrosion Layers," CORROSION/96, paper no. 4 (Houston, TX: NACE, 1996).